Nonequilibrium Thermomechanical Modeling of Liquid Drainage/Imbibition in Trickle Beds

I. Iliuta, M. Hamidipour, and F. Larachi
Dept. of Chemical Engineering, Laval University, Québec, Canada, G1V 0A6

DOI 10.1002/aic.12803
Published online December 7, 2011 in Wiley Online Library (wileyonlinelibrary.com).

We extend the macroscopic nonequilibrium thermomechanical multiphase flow theory proposed by Hassanizadeh and Gray for porous media to analyze a set of drainage and imbibition experiments in trickle beds. The nonequilibrium model rests on inclusion of mass and momentum conservations for the gas-liquid interface, nonequilibrium capillary pressure, Helmholtz free energy gradients in the body supply of momentum for fluid bulk phases and gas-liquid interface, and mass exchange rates between interface and fluid bulks accounting for production and destruction of gas-liquid interfacial area. To solve the nonequilibrium model, entropy-consistent constitutive relationships are derived and calibrated using liquid holdup and bed pressure drop measurements in drainage and imbibition. The model captures very well the decay (drainage), and breakthrough (imbibition) curvatures of liquid holdup and pressure drop kinetics, while model closer inspection allows assessing the role of nonequilibrium capillary pressure and of dynamic interfacial mass exchanges for the production/destruction of interfacial area. © 2011 American Institute of Chemical Engineers *AIChE J,* 58: 3123–3134, 2012
Keywords: trickle bed, drainage imbibition, nonequilibrium capillary pressure, Helmholtz free energy, gas-liquid interfacial area, thermomechanical modeling, electrical capacitance tomography

Introduction

Trickle-bed reactors consist of porous media in which gas and liquid compete for pore space in forced cocurrent downward flows. Already used for many decades in diverse engineering fields to host myriad gas-liquid–solid physical and chemical operations,[1] trickle beds are not to go out of fashion soon; and as academic objects, they still conceal challenging research problems. By venturing outside the comfort zone of traditional trickle-bed operations, researchers have reported that flow modulation, or per se the *transient state* it gives rise to, is at the origin of unprecedented behaviors acknowledged to lead to chemical and physical enhanced performances.

Application of flow modulation, first credited to Gupta,[2] demonstrated how dry spots and partial wetting can be prevented in trickle beds when liquid pulses wet and rewet the catalyst surface in a *perpetual* transient state. Many different flow modulation modes were afterward explored for promoting chemical reactions[3–7] via mass-transfer enhancements of the limiting reactants[8] or for improving physical processes, such as in the mitigation of filtration[9] or for the reduction of foaming.[10]

Studies entirely devoted to trickle-bed hydrodynamics in nonsteady state are relatively recent, and for the majority, purely experimental. By far, liquid flow rate modulation is a mode the literature mostly scrutinized whereby liquid pulse-base (or max-min), and base-pulse (or min-max), respectively, reminiscent of drainage and imbibition, are prompted in a periodic manner. The first detailed investigations were by Boelhouwer et al.[11] where liquid holdup characteristics (shock wave velocity, frequency, and morphology) were measured in slow and fast liquid flow modulation. Dependences of liquid pulse morphology were then thoroughly addressed with regard to particle size, feed frequency, temperature and pressure, in particular in the studies of Boelhouwer et al.[11], Giakoumakis et al.[12], Aydin et al.[13,14] and Aydin and Larachi.[15]

Four morphological descriptors fully characterize the dynamic evolution of liquid holdup in liquid flow rate modulation (Figure 1) (1) the breakthrough time which measures the transient time for the liquid holdup to rise from base to pulse level subsequent to min-max transition, (2) the decay time which corresponds to the time elapsed for the liquid holdup to retrieve back its base level subsequent to max-min transition, (3) the plateau time which measures the duration liquid holdup remains constant between breakthrough and decay interludes, and (4) the base-pulse amplitude which measures the increment of liquid holdup between base and pulse levels.

The dynamics of drainage and imbibition in trickle beds influences the morphology of pulses in liquid cyclic modulation. It is, therefore, sound to presume that comprehensive modeling of cyclic modulation cannot afford skipping the efforts for deriving reliable mathematical representations of the mechanisms subtending the breakthrough and decay segments of liquid pulses. Current literature status in the arena of modeling nonsteady-state trickle-bed hydrodynamics remains fairly shallow.[16,17] Rendition of liquid pulse morphology by means of *standard* two-phase flow models, i.e.,

Correspondence concerning this article should be addressed to F. Larachi at faical.larachi@gch.ulaval.ca.

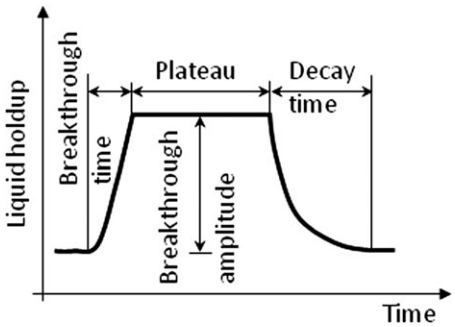

Figure 1. Illustration of the parameters characterizing: (a) morphological features of liquid holdup under cycled liquid feed.

Eulerian multifluid treatments, of trickle-bed hydrodynamics in nonsteady state has been recognized to be poor. Janecki et al.[16] simulations of liquid holdup time series revealed discrepancies between measured and computed breakthrough and decay times, and biased baseline holdups and oscillations. Atta et al.[17] in an attempt to describe as a prelude to modeling fast and slow cyclic modulation, the fate of solitary liquid waves in trickle beds did not accomplish better. The physics conveyed by the standard two-phase flow models is minimalistic as it relies on a set of mass and momentum balance equations for the gas and liquid bulk phases as well as *ad hoc* drag force relationships. We state that such physics is deficient because it insufficiently describes the role and presence of interfaces in the nonequilibrium conditions of drainage and imbibition.

In this work, a rigorous mathematical description of drainage and imbibition will be attempted by adapting the macroscopic nonequilibrium thermomechanical theory developed by Hassanizadeh and Gray[18] for multiphase flows in porous media. In this nonequilibrium thermomechanical theory, the interfaces and their thermodynamic properties are explicitly taken into account and treated as individual continua interacting and exchanging properties with the adjacent phase continua. The explicit inclusion of interfaces and interfacial properties is essential because they are known to have a significant role in determining the thermodynamic state of the whole system. This leads to the establishment of two categories of conservation equations whose *macroscopic* properties are defined at the scale of a representative elementary volume: one for the macroscopic bulk phase properties, i.e., as in the standard model, and another for the macroscopic *interfacial* properties. The nonequilibrium two-phase flow model will be built based on the following physical considerations (1) conservation equations for gas-liquid interfacial area and interfacial momentum, (2) nonequilibrium capillary pressure, (3) Helmholtz free energy gradients in the body supply of momentum for fluid bulk phases and gas-liquid interface, and (4) mass exchange between interface and adjacent fluid bulk phases accounting for the production/destruction of gas-liquid interfacial area in the course of imbibition and drainage.

Macroscopic 1-D (One-Dimensional) Balance Equations

For permanently fully wetted beds, i.e., absence of triple-phase curve, the system reduces to five superposed continua: three phases $\mathbf{V_l}$, $\mathbf{V_g}$, $\mathbf{V_s}$, and two interfaces $\mathbf{A_{gl}}$ and $\mathbf{A_{ls}}$ as sketched in Figure 2a. From this assumption, only $\mathbf{A_{gl}}$ is subject to variations in time and position whereas $\mathbf{A_{ls}}$ exhibits a *constant* liquid–solid contacting area, a_{ls}. This view differs in many aspects from the standard Eulerian multifluid treatments of trickle-bed hydrodynamics. Here, the main feature of the two-phase flow model rests on the inclusion of transport equations for the gas-liquid interfacial area. The model also includes mass-transfer exchange between the interface and its adjacent two bulk phases for accounting for the production/destruction of gas-liquid interfacial area in the course of imbibition and drainage steps in the trickle bed (Figure 2b).

The formalism of the conservation equations for these five continua is inspired from the general forms derived by Gray and Hassanizadeh[19] and adapted to our trickle-bed geometry assuming Newtonian unidirectional 1-D (streamwise), and isothermal (local thermal equilibrium) immiscible (no mass-transfer exchange between *bulk* phases) gas-liquid flows in a nondeformable and homogeneous (constant bed porosity) porous medium. The justification for each terms in the

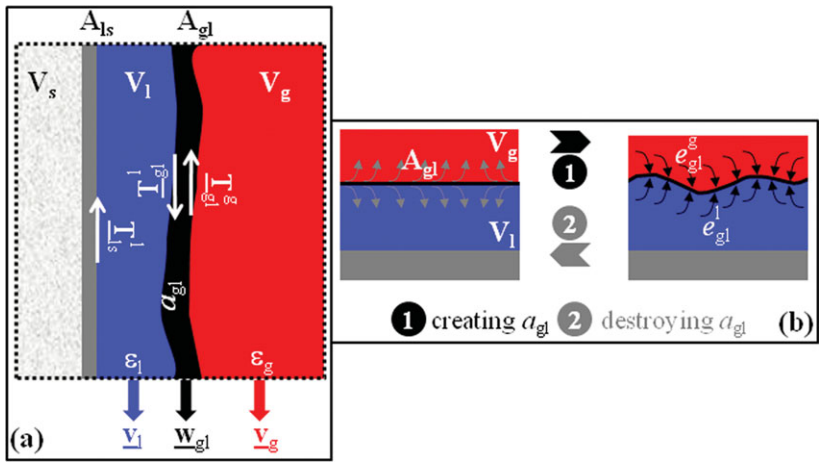

Figure 2. Representation of connectivity between subregions in the representative elementary volume: V_g, V_l, V_s for the bulk phases, A_{gl} and A_{ls} for the interfaces (a), interaction of interface A_{gl} with V_g and V_l, bulk phases in creating and destroying gas-liquid interfacial area (b).

[Color figure can be viewed in the online issue, which is available at wileyonlinelibrary.com.]

conservation equations, in particular the use of the momentum and continuity conservations for the gas-liquid and liquid–solid interfaces, is discussed at length in Hassanizadeh and Gray[18] and Gray and Hassanizadeh.[19] Hence, the model *per se* contains two categories of conservation equations whose *macroscopic* properties are defined at the scale of a representative elementary volume: one for the macroscopic bulk phase properties, and another for the macroscopic *interfacial* properties.[18,19]

Gas bulk conservation of mass

$$\frac{\partial}{\partial t}\left(\rho_g \varepsilon_g\right) + \frac{\partial}{\partial z}\left(\rho_g \varepsilon_g v_g\right) = e^g_{gl} \tag{1}$$

Liquid bulk conservation of mass

$$\frac{\partial}{\partial t}\left(\rho_l \varepsilon_l\right) + \frac{\partial}{\partial z}\left(\rho_l \varepsilon_l v_l\right) = e^l_{gl} \tag{2}$$

Gas-liquid interface conservation of mass

$$\frac{\partial}{\partial t}\left(\Gamma_{gl} a_{gl}\right) + \frac{\partial}{\partial z}\left(\Gamma_{gl} a_{gl} w_{gl}\right) = -e^g_{gl} - e^l_{gl} \tag{3}$$

Gas-bulk conservation of momentum

$$\rho_g \varepsilon_g \left(\frac{\partial v_g}{\partial t} + v_g \frac{\partial v_g}{\partial z}\right) + \frac{\partial}{\partial z}\left(\varepsilon_g P_g - \varepsilon_g \mu^e_g \frac{\partial v_g}{\partial z}\right) - \rho_g \varepsilon_g g = e^g_{gl} v_g + T^g_{gl} \tag{4}$$

Liquid bulk conservation of momentum

$$\rho_l \varepsilon_l \left(\frac{\partial v_l}{\partial t} + v_l \frac{\partial v_l}{\partial z}\right) + \frac{\partial}{\partial z}\left(\varepsilon_l P_l - \varepsilon_l \mu^e_l \frac{\partial v_l}{\partial z}\right) - \rho_l \varepsilon_l g = e^l_{gl} v_l + T^l_{gl} + T^l_{ls} \tag{5}$$

Gas-liquid interface conservation of momentum

$$\Gamma_{gl} a_{gl} \left(\frac{\partial w_{gl}}{\partial t} + w_{gl} \frac{\partial w_{gl}}{\partial z}\right) - \frac{\partial}{\partial z}\left(\gamma_{gl} a_{gl}\right) - \Gamma_{gl} a_{gl} g = - e^g_{gl}\left(v_g - w_{gl}\right) - e^l_{gl}\left(v_l - w_{gl}\right) - T^g_{gl} - T^l_{gl} \tag{6}$$

Solid bulk + solid–liquid interface conservation of momentum

$$-\frac{\partial}{\partial z}\left((1-\varepsilon)P_s\right) - (1-\varepsilon)\rho_s g + R_s - a_{ls}\Gamma_{ls} g = -T^l_{ls} \tag{7}$$

Volume conservation

$$\varepsilon_l + \varepsilon_g = \varepsilon \tag{8}$$

In Eqs. 1–8, v_α, P_α and ϵ_α are, respectively, the macroscopic interstitial velocity, pressure and holdup for the bulk α-phase ($\alpha = g$, l or s), w_{gl} is the macroscopic velocity of the gas-liquid interface, a_{gl} is the gas-liquid interfacial area per unit reactor volume, $\Gamma_{\alpha\beta}$ ($\alpha\beta = gl$ and ls) stands for the surface excess mass density per unit area of, respectively, the gas-liquid and the liquid–solid interfaces, γ_{gl} is the macroscopic interfacial tension of the gas-liquid interface, μ^e_α, is the α-phase macroscopic effective viscosity accounting for viscosity and spatial-fluctuation pseudo-turbulent dispersion, e^α_{gl} designates the mass exchange rates from the α ($= g$ or l) bulk phase to the gas-liquid interface, and $T^\alpha_{\alpha\beta}$ is the body supply of momentum to the α ($= g$ or l) bulk phase from the $\alpha\beta$ ($= gl$ or ls) interface. All the exchange terms can be recognized from the combination of superscript α ($= g$ or l) and subscript $\alpha\beta$ ($= gl$ or ls) to account for the property transfer from the $\alpha\beta$ interface to the contiguous bulk α-phase.

The immiscibility assumption in this treatment considers a fully passive two-phase flow excluding usual mass-transfer processes between *bulk* phases, such as phase change or solute diffusion across the gas-liquid interface. Therefore, the mass exchange rates, e^l_{gl} and e^g_{gl}, between the interface and the adjacent gas and liquid bulk phases are introduced to account for the production and destruction of gas-liquid interfacial area as a result of temporal changes of liquid holdup during dynamic stimulation of the trickle bed, i.e., drainage and imbibition.

To solve the previous conservation equations, Eqs. 1–8, the model 14 unknowns are divided into 8 primary variables (ϵ_g, ϵ_l, a_{gl}, v_g, v_l, w_{gl}, P_g, P_l) and 6 dependent variables (P_s, T^g_{gl}, T^l_{gl}, T^l_{ls}, e^l_{gl}, e^g_{gl}). For the system to become fully determinate, the six latter unknowns require functional dependences in the form of constitutive relationships to be elaborated by relating them to some of the primary variables.

In casting the constitutive relations for a gas-liquid flow through a *motionless* porous medium, only the macroscopic Helmholtz free energies per unit mass for the gas and liquid phases, and the gas-liquid interface, respectively, A_g, A_l and A_{gl}, are required.[18] *Ad hoc* constitutive relations for the macroscopic Helmholtz free energies are nonexistent in the context of trickle beds. To describe the thermodynamic state of the gas and liquid phases and the gas-liquid interface, they need to be formulated. Considering ϵ and a_{ls} (full bed wetting) are constant, the general dependences conjectured by Gray and Hassanizadeh[20] for the macroscopic Helmholtz free energies reasonably reduce to

$$A_{gl} = A_{gl}\left(a_{gl}, \varepsilon_l\right) \tag{9a}$$

$$A_l = A_l\left(a_{gl}, \varepsilon_l\right) \tag{9b}$$

$$A_g = A_g\left(a_{gl}, \varepsilon_l\right) \tag{9c}$$

These functional dependences highlight the role of interfacial area, a_{gl}, on the Helmholtz free energies as a macroscopic manifestation at the scale of the representative elementary volume of the microscopic curvature effects of the gas-liquid interface. Inclusion of a_{gl} as an independent variable to assess the impact of dynamic curvature phenomena on trickle-bed drainage and imbibition steps is possible because of the dedicated *interfacial* transport conservation equations, Eqs. 3 and 6.

Entropy Inequality

According to the principle of admissibility, the set of constitutive relationships must not violate the second law of thermodynamics, that is, whichever process a system is to be subjected to, the rate of net entropy production of the system must keep nonnegative.[18] A cautious approach advocated by Hassanizadeh and Gray[18] consists in building constitutive

relationships with the assumption that linearized nonequilibrium topological laws are inspired from the entropy inequality so that after substitution of the constitutive assumptions the second principle remains nontransgressed regardless of the system's thermodynamic state.

Hence, construction of the aforementioned macroscopic Helmholtz free energies will require that the terms in the following inequalities contribute to the production of entropy[20]

$$\frac{\partial \varepsilon}{\partial t}\left(\frac{\varepsilon_l}{\varepsilon}\rho_l^2\frac{\partial A_l}{\partial \rho_l}+\frac{\varepsilon_g}{\varepsilon}\rho_g^2\frac{\partial A_g}{\partial \rho_g}-P_s-\underbrace{\left(\rho_l\varepsilon_l\frac{\partial A_l}{\partial \varepsilon}+\rho_g\varepsilon_g\frac{\partial A_g}{\partial \varepsilon}+\Gamma_{gl}a_{gl}\frac{\partial A_{gl}}{\partial \varepsilon}\right)}_{\text{Void potential}}\right)\geq 0 \tag{C1}$$

$$\frac{\partial \varepsilon_l}{\partial t}\left(\rho_l^2\frac{\partial A_l}{\partial \rho_l}-\rho_g^2\frac{\partial A_g}{\partial \rho_g}-\rho_l\varepsilon_l\frac{\partial A_l}{\partial \varepsilon_l}+\rho_g\varepsilon_g\frac{\partial A_g}{\partial \varepsilon_g}-\Gamma_{gl}a_{gl}\frac{\partial A_{gl}}{\partial \varepsilon_l}\right)\geq 0 \tag{C2}$$

By recognizing that $P_\alpha = \rho_\alpha^2 \partial A_\alpha/\partial \rho_\alpha$, these inequalities can be approximated in nonequilibrium conditions by means of the following linearized topological laws

$$\frac{1}{\Pi_\varepsilon}\frac{\partial \varepsilon}{\partial t}=\frac{\varepsilon_l}{\varepsilon}P_l+\frac{\varepsilon_g}{\varepsilon}P_g-P_s-\rho_l\varepsilon_l\frac{\partial A_l}{\partial \varepsilon}-\rho_g\varepsilon_g\frac{\partial A_l}{\partial \varepsilon}-\Gamma_{gl}a_{gl}\frac{\partial A_{gl}}{\partial \varepsilon} \tag{10}$$

$$\frac{1}{\Pi_l}\frac{\partial \varepsilon_l}{\partial t}=P_l-P_g-\rho_l\varepsilon_l\frac{\partial A_l}{\partial \varepsilon}+\rho_g\varepsilon_g\frac{\partial A_s}{\partial \varepsilon_g}-\Gamma_{gl}a_{gl}\frac{\partial A_{gl}}{\partial \varepsilon_l} \tag{11}$$

where Π_ϵ and Π_l in Eqs. 10 and 11 are material proportionality coefficients constrained to be nonnegative by the entropy inequality.

Constitutive equations

• *Macroscopic solid pressure*. Through assumption of constant bed porosity, the void fraction potential is zero.[20] Therefore, Eq. 10 leads to the commonly accepted relationship that the macroscopic solid pressure is barycentric with respect to the saturation-weighted macroscopic gas and liquid pressures:

$$P_s=\frac{\varepsilon_l}{\varepsilon}P_l+\frac{\varepsilon_g}{\varepsilon}P_g \tag{12}$$

• *Momentum exchange terms*. The structure of the momentum exchange terms, $T^\alpha_{\alpha\beta}$, is suggested from an analysis of the entropy inequality to fulfill the restrictions that at equilibrium no relative movement of phases and interfaces is possible, i.e., v_α, w_{gl}, e^α_{gl}, $\partial \epsilon_\alpha/\partial t = 0$, and whereby the system's net entropy generation is minimal.[18] Assuming nonequilibrium states are near equilibrium, Taylor expansion of nonequilibrium equations about the equilibrium relations is applicable.[21] It follows that $T^\alpha_{\alpha\beta}$ in nonequilibrium state is formulated as the sum of surviving equilibrium and nonsurviving nonequilibrium (i.e., vanishing as v_α, $w_{gl} \to 0$) terms for the body momentum supply. The equilibrium terms are expressed as a function of the macroscopic Helmholtz free energies per unit mass, A_g, A_l and A_{gl},[18] whereas the nonequilibrium terms $\tau^\alpha_{\alpha\beta}$, are closed using drag expressions formulated for trickle-bed reactors[22]

$$T^g_{gl}=P_g\frac{\partial \varepsilon_g}{\partial z}-\rho_g\varepsilon_g\left(\frac{\partial A_g}{\partial a_{gl}}\frac{\partial a_{gl}}{\partial z}+\frac{\partial A_g}{\partial \varepsilon_l}\frac{\partial \varepsilon_l}{\partial z}\right)+\underbrace{\tau^g_{gl}}_{\text{non-equilibrium}} \tag{13a}$$

$$\tau^g_{gl}=-\alpha_{gl}\varepsilon_g^2\mu_g(2v_g-v_l)-\beta_{gl}\varepsilon_g^3\rho_g\left((v_g-v_l)^2+v_g^2\right) \tag{13b}$$

$$T^l_{gl}+T^l_{ls}=P_l\frac{\partial \varepsilon_l}{\partial z}-\rho_l\varepsilon_l\left(\frac{\partial A_l}{\partial a_{gl}}\frac{\partial a_{gl}}{\partial z}+\frac{\partial A_l}{\partial \varepsilon_l}\frac{\partial \varepsilon_l}{\partial z}\right)+\underbrace{\tau^l_{gl}+\tau^l_{ls}}_{\text{non-equilibrium}} \tag{14a}$$

$$\tau^l_{gl}+\tau^l_{ls}=\alpha_{gl}\varepsilon_g^2\mu_g(v_g-v_l)+\beta_{gl}\varepsilon_g^3\rho_g(v_g-v_l)^2-\varepsilon(\alpha_{ls}\mu_l+\beta_{ls}\rho_l\varepsilon_l v_l)v_l\varepsilon_l \tag{14b}$$

$$T^g_{gl}+T^l_{gl}=\Gamma_{gl}a_{gl}\frac{\partial A_{gl}}{\partial \varepsilon_l}\frac{\partial \varepsilon_l}{\partial z}+\underbrace{\tau^g_{gl}+\tau^l_{gl}}_{\text{non-equilibrium}} \tag{15a}$$

$$\tau^g_{gl}+\tau^l_{gl}=-\left(\alpha_{gl}\mu_g+\beta_{gl}\varepsilon_g\rho_g v_g\right)\varepsilon_g^2 v_g \tag{15b}$$

where

$$\alpha_{gl}=E_1\frac{(1-\varepsilon_g)}{\varepsilon_g^3 d_p^2}\left(\frac{1-\varepsilon}{1-\varepsilon_g}\right)^{2/3} \tag{16}$$

$$\beta_{gl}=E_2\frac{1-\varepsilon_g}{\varepsilon_g^3 d_p}\left(\frac{1-\varepsilon}{1-\varepsilon_g}\right)^{1/3} \tag{17}$$

$$\alpha_{ls}=E_1\frac{(1-\varepsilon)^2}{\varepsilon_l^3 d_p} \tag{18}$$

$$\beta_{ls}=E_2\frac{1-\varepsilon}{\varepsilon_l^3 d_p} \tag{19}$$

Each of Eqs. 13a, 14a, and 15a intervene in the momentum conservation Eqs. 4–6, respectively. The momentum exchange term, T^l_{ls}, in Eq. 7 can be obtained from combination of Eqs. 13a, 14a, and 15a.

It is worthy of notice that the momentum exchange terms (T^g_{gl}, T^l_{gl}, T^l_{ls}) would in turn determinate by requiring identification of the three Helmholtz functions. This leaves the

number of unknowns in the problem unchanged with same 8 primary variables and 6 dependent variables (P_s, A_{gl}, A_l, A_g, e^l_{gl}, e^g_{gl}).

• *Helmholtz free energy terms*. A full constitutive relationship for the Helmholtz free energy of the gas-liquid interface, A_{gl}, is not necessary for Eq. 9a as only knowledge of $\partial A_{gl}/\partial \epsilon_l$ is required in Eq. 15a. Provided the following equilibrium restriction is assumed[21]

$$-P_g + P_s - a_{gl}\Gamma_{gl}\frac{\partial A_{gl}}{\partial \varepsilon_l} = 0 \tag{20}$$

The term $\partial A_{gl}/\partial \epsilon_l$ can be expressed as a function of the primary variables by combining Eqs. 12 and 20

$$a_{gl}\Gamma_{gl}\frac{\partial A_{gl}}{\partial \varepsilon_l} = -\frac{\varepsilon_l}{\varepsilon}(P_s - P_l) \tag{21}$$

To construct an *ad hoc* constitutive expression for the Helmholtz free energy of the liquid phase A_1, the following limiting topological constraints have been speculated[23]

$$\varepsilon_l \frac{\partial A_l}{\partial \varepsilon_l} \geq 0 \text{ such that } \varepsilon_l \frac{\partial A_l}{\partial \varepsilon_l} = 0 \text{ as } \varepsilon_l = 0 \,\&\, \varepsilon \tag{C3}$$

$$a_{gl}\frac{\partial A_l}{\partial a_{gl}} \geq 0 \text{ such that } a_{gl}\frac{\partial A_l}{\partial a_{gl}} = 0 \text{ as } a_{gl} = 0 \tag{C4}$$

C3 states that invasion of the porous medium by the wetting phase $\mathbf{V_l}$—at the expense of the nonwetting phase $\mathbf{V_g}$—is accompanied by wetting heat effects which increase energy of the wetting phase as ϵ_l is increased, and the culmination of which is reached when the nonwetting phase would have been totally evacuated from the porous medium, i.e., $\epsilon_l \rightarrow \epsilon$. Similar topological behavior for the creation of the gas-liquid interfacial area (Eq. C4) is assumed. An empirical expression for A_l was proposed, following the dependence proposed by Gray and Hasssanizadeh,[20] by least-squares fit between our experimental data (liquid holdup and pressure drop as a function of time) and the simulated output from Eqs. 1–8, while meeting the constraints C1 and C2

$$A_l = -\beta\frac{P_l}{\rho_l}\left[1 - \frac{1}{\phi}\left(\frac{a_{gl}}{a_{ls}}\right)^{\phi}\right]\left(1 + \frac{\varepsilon_l^3}{3\varepsilon^2} - \frac{\varepsilon_l^2}{2\varepsilon}\right) \tag{22}$$

Expressions for $\partial A_l/\partial \epsilon_l$ and $\partial A_l/\partial a_{gl}$ needed in Eq. 14a are fully rendered from Eq. 22.

Finally, for establishing an expression for the Helmholtz free energy of the gas phase, A_g, Eq. 13a suggests that the *two* dependences of A_g with respect to a_{gl} and ϵ_l must be developed. For a formulation of the dependence with respect to a_{gl}, quasi-equilibrium in the interchange of energy via the gas-liquid interfacial area is assumed between the liquid and gas bulk phases such that one obtains from the entropy inequality[20]

$$\rho_g\varepsilon_g\frac{\partial A_g}{\partial a_{gl}} = -\rho_l\varepsilon_l\frac{\partial A_l}{\partial a_{gl}} \tag{23}$$

For the derivation of the dependence of A_g with respect to ϵ_l, the topological closure Eq. 10 was assumed on the basis of linearization of the term $\partial \epsilon_l/\partial t$ from the entropy inequality.[20] Following a similar decomposition as for the nonequilibrium body momentum supply, the nonequilibrium (or dynamic) capillary pressure $P_g - P_l$, can be formulated as the sum of surviving equilibrium and nonsurviving nonequilibrium terms so that Eq. 11 is reorganized as follows

$$P_g - P_l = \rho_g\varepsilon_g\frac{\partial A_g}{\partial \varepsilon_g} - \rho_l\varepsilon_l\frac{\partial A_l}{\partial \varepsilon_l} - \Gamma_{gl}a_{gl}\frac{\partial A_{gl}}{\partial \varepsilon_l} \underbrace{-\frac{1}{\Pi_l}\frac{\partial \varepsilon_l}{\partial t}}_{\text{non-equilibrium}} \tag{24}$$

The sum of the first three terms in Eq. 24 RHS represents the surviving *equilibrium* (or static) capillary pressure. The coefficient Π_l —dimensionally homogeneous to a reciprocal dynamic viscosity— is a measure of the system's response (or relaxation) to restore back equilibrium. Eq. 24 reduces to the well known *equilibrium* capillary pressure expression if sufficient time is allowed for equilibrium to be restored, i.e., $\partial \epsilon_\varkappa/\partial t = 0$ or if the system's relaxation time is very short ($1/\Pi_l = o(\partial \epsilon_l/\partial t)$):

$$\left(P_g - P_l\right)_{\text{eq.}} = P_c|_{\text{eq.}} = \left(\rho_g\varepsilon_g\frac{\partial A_g}{\partial \varepsilon_g} - \rho_l\varepsilon_l\frac{\partial A_l}{\partial \varepsilon_l} - \Gamma_{gl}a_{gl}\frac{\partial A_{gl}}{\partial \varepsilon_l}\right)\Bigg|_{\text{eq.}} \tag{25}$$

During a liquid pulse-base (or max-min) transition, the trickle bed undergoes liquid drainage ($\partial \epsilon_l/\partial t < 0$) whereby the dynamic capillary pressure $P_g - P_l$, is greater than the equilibrium capillary pressure (Eq. 25). Conversely, a liquid base-pulse (or min-max) transition entails $\partial \epsilon_l/\partial t > 0$ (i.e., imbibition), whereby the dynamic capillary pressure $P_g - P_l$, is lower than its equilibrium *alter ego*. Both policies satisfy positivity of the entropy inequality condition C2.[24]

Finally, merging Eq. 21 with Eq. 24 and rearranging yields the second relationship for A_g for this latter to become fully determined

$$\rho_g\varepsilon_g\frac{\partial A_g}{\partial \varepsilon_1} = -\frac{1}{\Pi_1}\frac{\partial \varepsilon_1}{\partial t} - \rho_1\varepsilon_1\frac{\partial A_1}{\partial \varepsilon_1} - \frac{\varepsilon_g}{\varepsilon}\left(P_g - P_1\right) \tag{26}$$

Note that recourse to empirical capillary relationships, such as the Leverett *J*-function, is no longer needed as this approach enables access to dynamic capillary pressure via entropy-consistent constitutive expressions for the macroscopic Helmholtz free energies. The functional dependences of the macroscopic Helmholtz free energies given by Eqs. 9b and c expose the fact that capillary pressure, both in its nonequilibrium (Eq. 24) or equilibrium (Eq. 25) form, is a function of two independent variables, liquid holdup and gas-liquid interfacial are, namely $P_c - \epsilon_l - a_{gl}$. This proposal contrasts with the trickle bed literature in which $P_c - \epsilon_l$ relationships are classically assumed and whose multivalued character is ascribed to hysteresis phenomena.[25,26] Although it was not the purpose of our study to include an investigation of hysteresis phenomena in trickle beds, the new functional formulations, $P_c - \epsilon_l - a_{gl}$, mean with the current formalism, there is no reason to *ascribe a multivalued character to some constitutive relations in the proposed*

because inclusion of gas-liquid interfacial area a_{gl}, erases indeed the "multivaluedness" artifact.

• *Mass exchange terms for production/destruction of* a_{gl}.To account for the creation and destruction of gas-liquid interfacial area during drainage and imbibition of the trickle bed, constitutive forms must be established for the mass exchange terms from the gas and liquid bulk phases to the gas-liquid interface, e^l_{gl} and e^g_{gl}. To set the functional forms for these mass-transfer rates, we adopt an intuitive approach on the basis of Niessner and Hassanizadeh[27,28] work

$$e^l_{gl} = \lambda(\rho_l, a_{gl}, \varepsilon_l)\frac{\partial \varepsilon_l}{\partial t} \tag{27}$$

$$e^g_{gl} = \lambda(\rho_l, a_{gl}, \varepsilon_l)\frac{\rho_g}{\rho_l}\frac{\partial \varepsilon_l}{\partial t} \tag{28}$$

Where e^α_{gl} ($\alpha = g, l$) is negative (respectively, positive) when gas-liquid interfacial area is created (respectively, destroyed). The functional parameter, λ, characterizes the strength of change of specific gas-liquid interfacial area due to a change in liquid holdup. This parameter is speculated to depend on the liquid holdup and gas-liquid interfacial area with the restrictions: $\lambda = 0$ for $a_{gl} = 0$ or $\epsilon_l = \epsilon$ or $\epsilon_l = \epsilon^*_l$ (when the generation of interfacial area is halted).

$$\lambda = -\alpha\rho_l\frac{a_{gl}}{a_{ls}}\left[1 - \frac{\varepsilon_l}{\varepsilon^*_l} - \left(\frac{\varepsilon^*_l - \varepsilon_l}{\varepsilon^*_l}\right)^2\right]\frac{u_{sl,p}}{u_{sl,b}} \qquad \varepsilon_l \le \varepsilon^*_l \tag{29a}$$

$$\lambda = \alpha\rho_l\frac{a_{gl}}{a_{ls}}\left[1 - \frac{\varepsilon - \varepsilon_l}{\varepsilon - \varepsilon^*_l} - \left(\frac{\varepsilon_l - \varepsilon^*_l}{\varepsilon - \varepsilon^*_l}\right)^2\right]\frac{u_{sl,p}}{u_{sl,b}} \qquad \varepsilon_l \ge \varepsilon^*_l \tag{29b}$$

In Eqs. 29a,b, ϵ^*_l (= 0.21 ϵ) is the liquid holdup corresponding to a maximum gas-liquid interfacial area[29] and $u_{sl,b}$ and $u_{sl,p}$ are, respectively, the base and pulse liquid superficial velocities imposed in the trickle bed. Parameter α was evaluated by least-squares fit between experimental data (liquid holdup and pressure drop as a function of time) and simulated model output.

According to Eq. 6, the gas-liquid interfacial area changes because of combined mass and body momentum exchange effects. Niessner and Hassanizadeh[27] embodied both phenomena in a single production rate term similar to Eq. 27 and which was included in a gas-liquid interface conservation of mass analogous to Eq. 3. Unlike these authors, Eqs. 27 and 28 in our study only account for the interconversion between gas-liquid interfacial area and bulk fluid holdups due to mass exchange effects, whereas the contribution from the body momentum exchange terms is handled via Eqs. 15a and b in Eq. 6.

One last remark is worth mentioning about the structure of the aforementioned constitutive mass-transfer rates. Gas bulk holdup would contribute by the same way as liquid bulk although much marginally as $\rho_g/\rho_l = o$ (1) in Eq. 28. However, by virtue of Eq. 9 both gas and liquid holdups cannot diminish simultaneously. This suggests our constitutive equation Eq. 28 is flawed. Nevertheless, as $e^g_{gl} = o(e^l_{gl})$, the role of mass exchange term e^g_{gl} is vanishingly small and can be taken equal to zero without consequences on the simulated trends.

• *Auxiliary constitutive relations and boundary conditions*. Provided auxiliary constitutive equations are supplemented for the property variables (γ_{gl}, Γ_{gl}, Γ_{ls}, μ^e_l, μ^e_g, ρ_g), the system of equations: Eqs. 1–8 with Eqs. 12, 21, 22, 23, 26–28, allows closure of the model for its 14 unknowns (ϵ_g, ϵ_l, a_{gl}, v_g, v_l, w_{gl}, P_g, P_l, P_s, A_{gl}, A_l, A_g, e^g_{gl}, e^l_{gl}).

The α-phase effective viscosity μ^e_α, arising from the combination of viscous and pseudo-turbulence stress tensors is formulated as proposed by Dankworth et al.[30] and the gas density is evaluated using the ideal gas law.

The macroscopic interfacial tension γ_{gl}, depends on the Helmholtz free energy of the gas-liquid interface A_{gl}, and is defined as[18]

$$\gamma_{gl} = -\Gamma_{gl}a_{gl}\frac{\partial A_{gl}}{\partial a_{gl}} \tag{30}$$

Applying to Eq. 9a the chain rule, one obtains[24]

$$\frac{\partial A_{gl}}{\partial \varepsilon_l} = -\frac{\partial A_{gl}}{\partial a_{gl}}\frac{\partial a_{gl}}{\partial \varepsilon_l} \tag{31}$$

In our treatment, γ_{gl} was computed in its reformulated form obtained by combining Eqs. 20 and 31 into Eq. 30 to yield

$$\gamma_{gl} = \frac{\varepsilon_1}{\varepsilon}\frac{\partial \varepsilon_1}{\partial a_{\mathrm{gl}}}\left(P_{\mathrm{l}} - P_{\mathrm{g}}\right) \tag{32}$$

The macroscopic surface excess mass density function Γ_{gl}, defined as the excess mass of gas-liquid interface divided by the total area of the interface was approximated under steady state, no gas-liquid mass transfer conditions and neglecting the advective terms in the 1-D model. Pressure drop was considered the only driving force for the flow and, therefore, the gradients of the Helmholtz free energies in bulk liquid and gas were assumed negligible. Under these assumptions, Eq. 6 reduces to

$$\gamma_{\mathrm{gl}}\frac{\partial a_{gl}}{\partial z} + \Gamma_{\mathrm{gl}}a_{\mathrm{gl}}g = \Gamma_{\mathrm{gl}}a_{\mathrm{gl}}\frac{\partial A_{\mathrm{gl}}}{\partial \varepsilon_{\mathrm{l}}}\frac{\partial \varepsilon_{\mathrm{l}}}{\partial z} + \tau^{\mathrm{g}}_{\mathrm{gl}} + \tau^{\mathrm{l}}_{\mathrm{gl}} \tag{33}$$

Combining Eqs. 31 and 32 into Eq. 33, one obtains

$$\Gamma_{gl} \approx \left.\frac{\tau^g_{gl} + \tau^l_{gl}}{a_{gl}g}\right|_{@\text{ steady state}} \tag{34}$$

A similar expression is evaluated for the excess mass of liquid–solid interface, Γ_{ls}, by writing simplified conservation of momentum for the solid–liquid interface (Eq. 35) and the solid bulk (Eq. 33)

$$\Gamma_{ls} \approx \left.\frac{\tau^l_{ls} + \tau^s_{ls}}{a_{ls}g}\right|_{@\text{ steady state}} \tag{35}$$

$$\tau^s_{ls} \approx \left.-\frac{\partial}{\partial z}((1-\varepsilon)P_s)\right|_{@\text{ steady state}} \tag{36}$$

Velocities at the inlet are specified as Dirichlet-type boundary conditions. Liquid holdup at reactor inlet is evaluated assuming steady state, no gas-liquid mass-transfer conditions, neglecting the advective terms and the gradients of the Helmholtz free energies in the 1-D model, and

Table 1. Experimental Trickle-Bed Operating Conditions

Bed diameter, m	0.057
Bed height, m	0.8
Particle diameter, m	0.003
Particle shape	Spherical glass bed
Bed porosity	0.395
Liquid phase	Kerosene
Gas phase	Air
Base/min liquid velocity, m/s	0.00065, 0.0013 and 0.002
Pulse/max liquid velocity, m/s	0.002, 0.0027
Gas velocity, m/s	0.062, 0.185
Pressure, bar	1
Temperature, K	298

considering pressure drop as the only driving force. Under these assumptions, the 1-D hydrodynamic model gives

$$\frac{\tau_{gl}^{l}}{\varepsilon_l}+\frac{\tau_{ls}^{l}}{\varepsilon_l}-\frac{\tau_{ls}^{g}}{\varepsilon-\varepsilon_l}+(\rho_l-\rho_g)g=0 \tag{37}$$

The gas-liquid interfacial area and the velocity of the gas-liquid interface at the reactor inlet are estimated using, respectively, neural network correlations[31] and the double slit model.[32] Outflow boundary conditions with zero gradients normal to outflow boundary for flow variables, except pressure, are used at the outlet.

With the experimental results obtained in this work, the following values for the fitted parameters α (Eqs. 29a and b.), β and ϕ (Eq. 22) and Π_l (Eq. 26) are found: $\alpha = 4.75$, $\beta = 1.21\ 10^{-2}$, $\phi = 3$ and $\Pi_l = 1\ \mathrm{m{\cdot}s{\cdot}kg^{-1}}$.

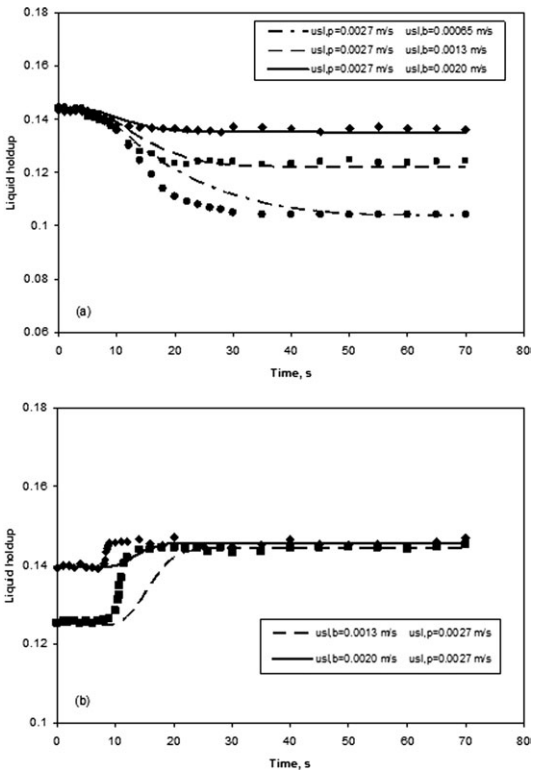

Figure 3. Experimental vs. predicted instantaneous liquid holdup profiles for max-min (a), and min-max (b) operation (H = 60 cm; u_{sg} = 0.185 m/s).

Standard two-phase flow model (1) no interfacial conservation equations, (2) equilibrium capillary pressure (3) no gradients of Hermholtz free energies in body supply of momentum, and (4) no mass exchange between gas-liquid interface and fluid bulk phases.

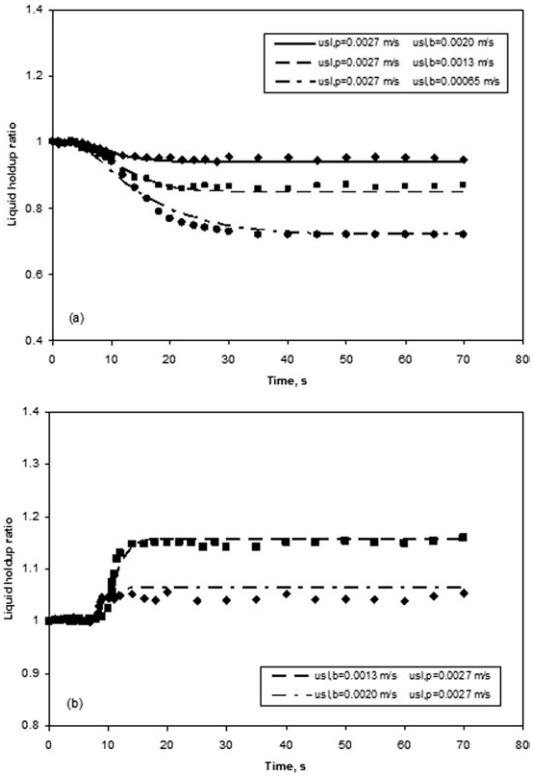

Figure 4. Experimental vs. predicted (nonequilibrium two-phase flow model) instantaneous liquid holdup (ϵ_l/ϵ_l (t = 0)) profiles for max-min (a) min-max (b) operation (H = 0.60 m; u_{sg} = 0.185 m/s).

Experimental

Liquid pulse-base or max-min (drainage) and base-pulse or min-max (imbibition) experiments were performed with air and kerosene at room temperature and atmospheric pressure (at bed exit) using a 5.7-cm-ID Plexiglas column. The column was packed up to a height of 80 cm with spherical glass beads, 3 mm in diameter, resulting in bed porosity of 0.395. The packing was maintained by means of a rigid stainless steel screen placed at the column bottom. Liquid was distributed through a spray nozzle to ensure even distribution. Air was entered through several small holes on the top of the bed. To achieve full bed prewetting, the packed bed was systematically operated in the pulse flow mode before setting the drainage and imbibition runs. The bed inlet pressure was measured at a frequency of 1 Hz.

A 12/12-electrode twin-plane electrical capacitance tomography (ECT) sensor (PTL300E with DAM200E sensor controller, Process Tomography, Ltd.) with axial sliding capability was used for quantifying and monitoring the liquid holdup dynamics. The ECT scanner was mounted on a sleeve and could slide over the reactor outer diameter for interrogation of any axial region of the vessel. ECT scans were performed at bed elevations 60 and 65 cm from top during drainage and imbibition tests. The measured capacitances (66 independent sets) were used to reconstruct mixture permittivity distribution out of which instantaneous per-pixel phase saturations (32 × 32 pixels per image) were

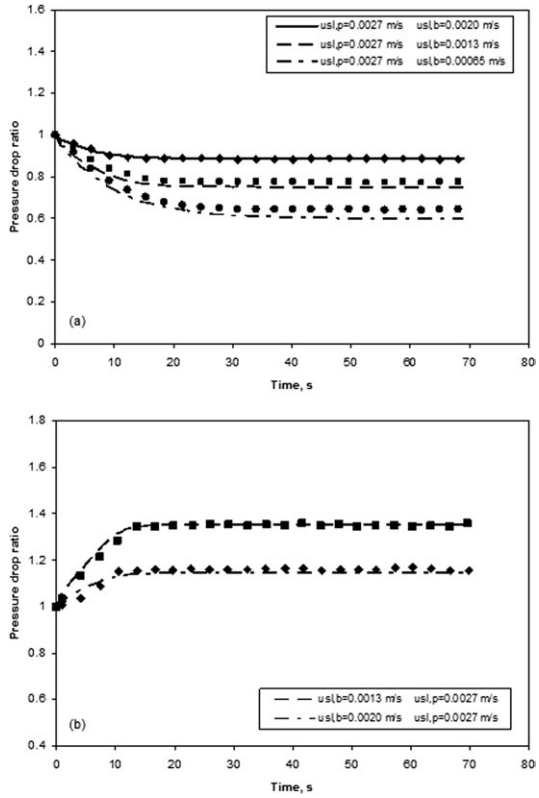

Figure 5. Experimental vs. predicted (nonequilibrium two-phase flow model) instantaneous pressure drop ($\Delta P/\Delta P_l$ (t = 0)) profiles for max-min (a) min-max (b) operation (H = 0.60 m; u_{sg} = 0.185 m/s).

extracted following procedures validated in our previous works.[33,34] The ECT instantaneous images were then converted into cross-sectionally averaged instantaneous liquid holdups. Typical sampling frequency corresponds to 50 tomographic scans per second.

The experimental conditions are summarized in Table 1. Two-pulse (max) liquid superficial velocities, 2.0 10^{-3} m/s and 2.7 10^{-3} m/s were used while base (min) liquid superficial velocities were allowed to vary between 6.5 10^{-4} and 2 10^{-3} m/s. Two-gas superficial velocities were imposed in all explored cases.

Results and Discussion

• *Standard two-phase flow model*. Preliminary simulations consisted in assessing the pertinence of deploying nonequilibrium thermomechanical multiphase models for a description of unsteady state trickle-bed hydrodynamics such as for drainage or imbibition. Liquid drainage and imbibition dynamic curves ϵ_l vs. time measured for different ($u_{sl,b}$, $u_{sl,p}$) sets are compared to simulations from the so-called *standard* two-phase flow model. By standard model, the following assumptions are meant (1) interfacial conservation equations are ignored, (2) equilibrium capillary pressure is established instantaneously (Eq. 25 is fulfilled in all times), (3) pressure drop is the only driving force for the flow so that gradients of the Helmholtz free energies in the body supply of momentum are neglected, (4) mass exchange from the gas-liquid interface to the gas or liquid phase is not considered (e^{α}_{gl} = 0). In this standard model, the set of primary variables is reduced to (ϵ_g, ϵ_l, v_g, v_l, P_g, P_l) which are obtained from solving the conservation equations Eqs. 1, 2, 4, 5, 8, and 25, where the equilibrium capillary pressure (Eq. 25) is approximated by means of the Leverett J-function[35] and P_s is estimated from Eq. 12. A typical set of numerical comparisons for max-min and min-max operation is illustrated in Figure 3 for $u_{g,s}$ = 0.185 m/s. Capture by the standard model of the steady-state liquid holdups before and after drainage/imbibition is very good. However, it is evident from these comparisons, that the standard hydrodynamic model is unable to capture satisfactorily the curvature of the liquid drainage and imbibition curves. The standard model predicts much slower deformations in shape of the ϵ_l vs. time curves, especially as

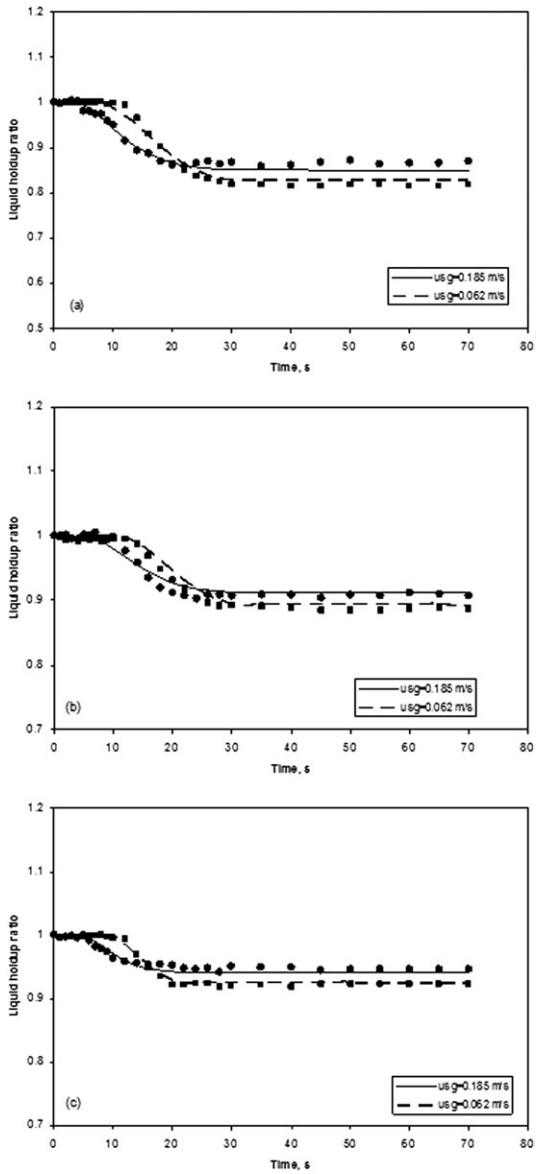

Figure 6. Effect of superficial gas velocity on experimental vs. predicted (nonequilibrium two-phase flow model) instantaneous liquid holdup (ϵ_l/ϵ_l (t = 0)) profiles for max-min operation (H = 0.65 m), (a) $u_{sl,p}$ = 0.0027 m/s, $u_{sl,b}$ = 0.0013 m/s, (b) $u_{sl,p}$ = 0.002 m/s, $u_{sl,b}$ = 0.0013 m/s, and (c) $u_{sl,p}$ = 0.0027 m/s, $u_{sl,b}$ = 0.002 m/s.

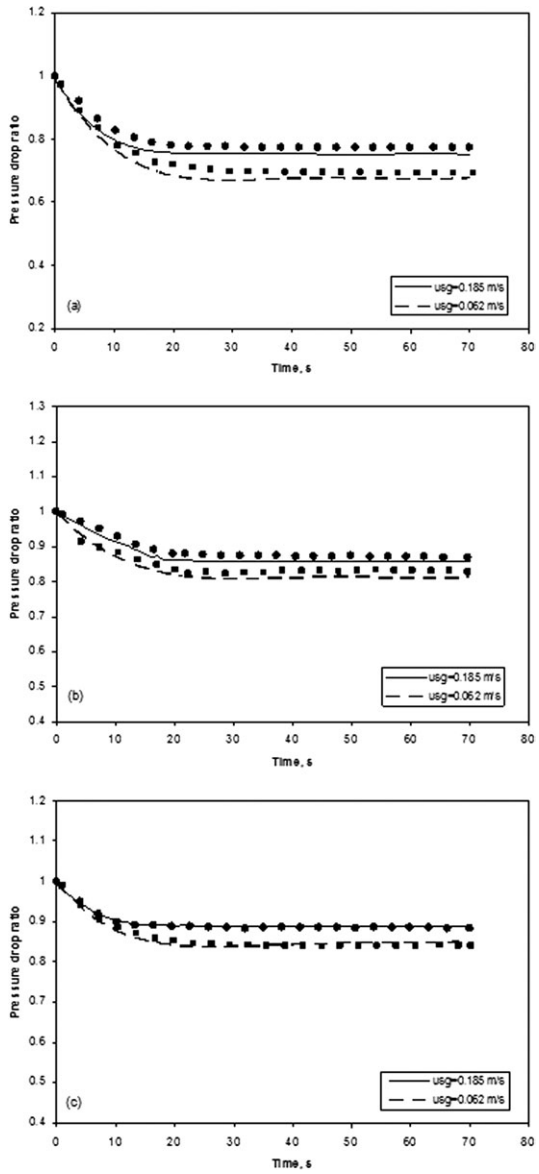

Figure 7. Effect of superficial gas velocity on experimental vs. predicted (nonequilibrium two-phase flow model) instantaneous pressure drop ($\Delta P/\Delta P_l$ (t = 0)) profiles for max-min operation (a) $u_{sl,p}$ = 0.0027 m/s, $u_{sl,b}$ = 0.0013 m/s, (b) $u_{sl,p}$ = 0.002 m/s, $u_{sl,b}$ = 0.0013 m/s, and (c) $u_{sl,p}$ = 0.0027 m/s, $u_{sl,b}$ = 0.002 m/s.

the contrast between $u_{sl,b}$ and $u_{sl,p}$ deepens resulting in measured deformations that become more and more pronounced.

• *Nonequilibrium thermomechanical two-phase flow model*. The experimental liquid holdup and pressure drop data are subsequently compared to simulations from the complete nonequilibrium model (Eqs. 1–8, 12, 21, 22, 23, and 26–28). Experimental and simulated instantaneous liquid holdup ratio ($\epsilon_l/\epsilon_l(t = 0)$) profiles are compared for max-min (Figure 4a) and min-max (Figure 4b) runs and different ($u_{sl,b}$, $u_{sl,p}$) sets as indicated in Table 1. For an identical ($u_{sl,b}$, $u_{sl,p}$) pair, the decay time of drainage curves (Figure 4a) is larger than the breakthrough time of imbibition curves (Figure 4b). Decay times slacken as the contrasts between $u_{sl,p}$ and $u_{sl,b}$ widen. This is unlike the breakthrough times which remain barely influenced by the gap between $u_{sl,b}$ and $u_{sl,p}$. If *waterflood* fronts (in imbibition) arrive suddenly, their rears (in drainage), on the contrary, retreat slowly as reflected in the absence of symmetry of traveling solitary waves[17] or of liquid pulse shapes in cyclic modulation.[13] Not only the model is able to distinguish between different breakthrough and decay times for liquid holdup, it also captures very well the sharper imbibition curvatures. Hence, inclusion of *interfacial* mass and momentum balance equations along with Helmholtz free energies and nonequilibrium capillary pressure improves model aptness to describe the transient hydrodynamics much better than the standard model. Similar remarks can be drawn from a comparison between measured and simulated pressure drops during drainage (Figure 5a) or imbibition (Figure 5b). The time scales in pressure stabilization follow the same trends as for liquid holdup. However, the pressure curves imbed the dynamics of the whole bed unlike the liquid holdup measurements which reflect the local environment sensed via ECT at 60 cm bed depth. The influence of superficial gas velocities on drainage and imbibition dynamics is illustrated in Figures 6–9. These figures compare experimental and predicted instantaneous liquid holdup and pressure drop ratio profiles, respectively, for three ($u_{sl,b}$, $u_{sl,p}$) sets in max-min (Figures 6 and 7), and min-max (Figures 8 and 9) conditions. Regardless of the prevailing $u_{g,s}$, full drainage and imbibition histories of liquid holdup and pressure drop variations are well described by the nonequilibrium model. The model expectably captures the shorter response times with increased

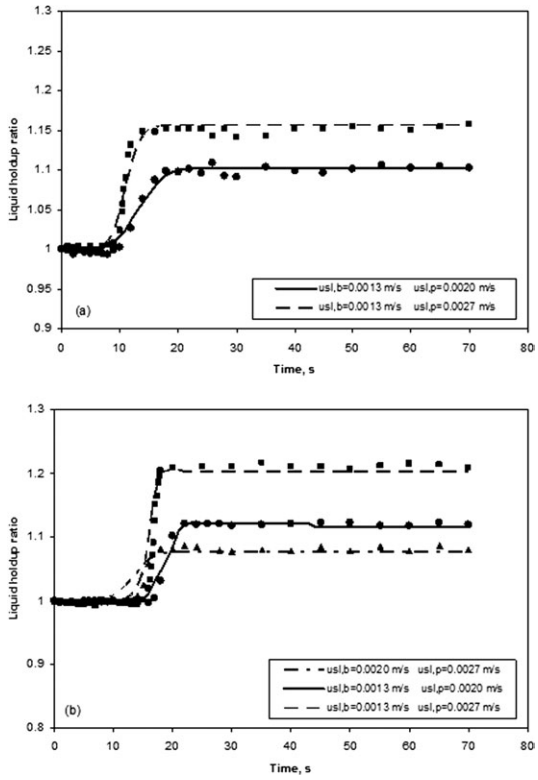

Figure 8. Effect of superficial gas velocity on experimental vs. predicted (nonequilibrium two-phase flow model) instantaneous liquid holdup (ϵ_l/ϵ_l (t = 0)) profiles for min-max operation (H = 0.65 m) (a) u_{sg} = 0.185 m/s, and (b) u_{sg} = 0.062 m/s.

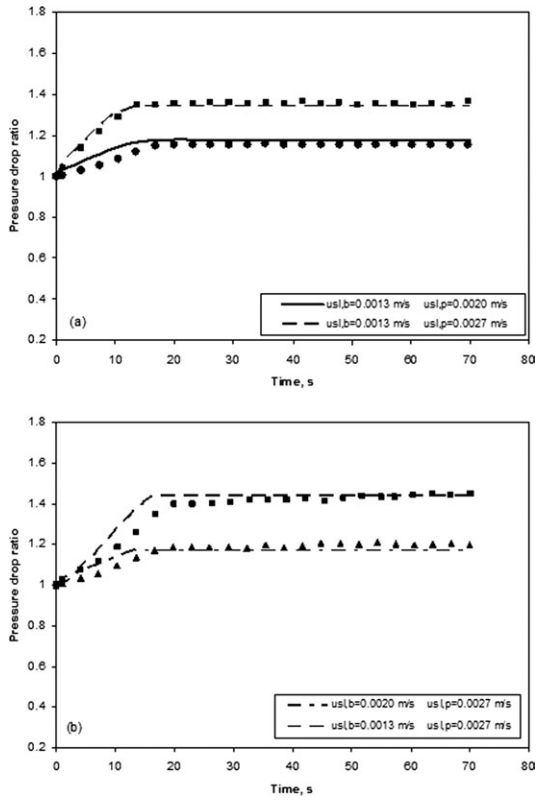

Figure 9. Effect of superficial gas velocity on experimental versus predicted (nonequilibrium two-phase flow model) pressure drop ($\Delta P/\Delta P_l$ (t = 0)) profiles for min-max operation (a) u_{sg} = 0.185 m/s, and (b) u_{sg} = 0.062 m/s.

superficial gas velocities of liquid holdup drainage (Figure 6) and imbibition (Figure 8). Furthermore, the independence of liquid holdup decay (Figure 6), and breakthrough (Figure 8) times with respect to superficial gas velocity are also predicted by the nonequilibrium model. In the case of pressure drop ratio, both decay (Figure 7) and breakthrough (Figure 9) times decrease with the raise of the gas superficial velocity.

• *Role of mass exchange terms for production/destruction of a_{gl}.* Let us examine the model sensitivity to interconversion between gas-liquid interfacial area and bulk fluid holdups due to mass exchange effects (e^l_{gl} and e^g_{gl} via Eqs. 27 and 28). Liquid holdup profiles simulated during drainage and imbibition for 0.1 MPa (Figure 10a) and 0.8 MPa (Figure 10b) at bed elevation $H = 0.65$ m are illustrated for two values of parameter α: $\alpha = 0$ ($\lambda = 0$) and $\alpha = 4.75$. In the latter case, non-negative λ values are computed from Eq. 29b as ϵ_l is always greater than ϵ^*_l for Figure 10 simulations. Changes of gas-liquid interfacial area when $\alpha = 0$ result only from alteration of the body momentum exchange terms, T^g_{gl} and T^l_{gl}, in Eq. 6, whereas mass conservation of interface tells a_{gl} is transported *passively* via Eq. 6 ($e^\alpha_{gl} = 0$). As can be judged from Figure 10, the mass exchange terms (e^l_{gl} and e^g_{gl} via Eqs. 27 and 28), between bulk fluid phase holdups and gas-liquid interfacial area play a nonnegligible role in the drainage and imbibition dynamics alike. By accounting for the production/destruction of a_{gl} (λ from Eq. 29b), these terms prompt much briefer response times for the system to attain steady state in comparison to the case $\alpha = 0$. Furthermore, the dynamics of transition between steady states becomes more gradual at elevated pressures. Under max-min conditions, e^α_{gl} ($\alpha = g, l$) are negative since $\partial\epsilon_l/\partial t < 0$ and $\lambda > 0$ ($\alpha = 4.75$). Therefore, gas-liquid interfacial area is generated due to mass exchanges from the bulk phases to the gas-liquid interface. This contributes to a further depletion of bulk liquid holdup by routing toward the interface additional liquid molecules. The result is an accelerated drop in liquid holdup in accordance with Figure 10 trends. For much like the same reason, by imposing min-max conditions e^α_{gl} ($\alpha = g, l$) become positive since $\partial\epsilon_l/\partial t > 0$ and $\lambda > 0$ ($\alpha = 4.75$). Gas-liquid interfacial area is destroyed during imbibition driving back more liquid molecules toward the liquid-bulk phase. Enrichment by this mechanism of the bulk liquid entrains a precocious breakthrough in liquid holdup as compared to the case $\alpha = 0$ (Figure 10).

• *Equilibrium vs. nonequilibrium macroscopic capillary pressure.* Another feature worth addressing in the nonequilibrium model rests on assessing which macroscopic capillary pressure, nonequilibrium or equilibrium, is physically sound. Figure 11 illustrates the instantaneous behavior of the ratio of dynamic to static capillary pressures, $(P_g - P_l)/P_c$, for drainage and imbibition steps at different reactor pressures at bed elevation $H = 0.65$ m. The dynamic capillary pressure is obtained by subtracting the instantaneous pressures resulting from solving the nonequilibrium model. The static capillary pressure is calculated as $\rho_g\epsilon_g\partial A_g/\partial\epsilon_g - \rho_l\epsilon_l\partial A_l/\partial\epsilon_l -$

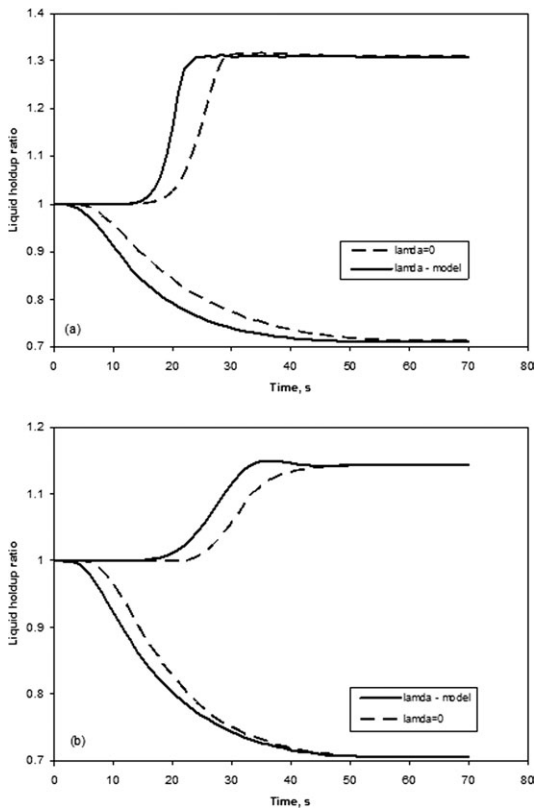

Figure 10. Model sensitivity to interconversion between gas-liquid interfacial area and liquid holdup (λ = 0 and λ from Eq. 29b).

Liquid holdup ratio profiles in drainage and imbibition steps at H = 0.65 m. (a) P = 0.1 MPa, $u_{sl,p}$ = 0.0027 m/s, $u_{sl,b}$ = 0.00065 m/s (max-min), $u_{sl,b}$ = 0.00065 m/s, $u_{sl,p}$ = 0.00195 m/s (min-max), (b) P = 0.8 MPa, $u_{sl,p}$ = 0.0027 m/s, $u_{sl,b}$ = 0.00065 m/s (max-min), $u_{sl,b}$ = 0.00065 m/s, $u_{sl,p}$ = 0.0011 m/s (min-max).

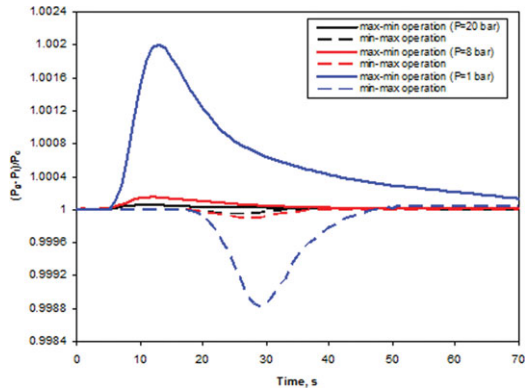

Figure 11. Ratio of dynamic capillary pressure $P_g - P_l$, to static capillary pressure $P_c = \rho_g \epsilon_g \partial A_g/\partial \epsilon_g - \rho_l \epsilon_l \partial A_l/\partial \epsilon_l - \Gamma_{gl} a_{gl} \partial A_{gl}/\partial \epsilon_l$ for $u_{sl,p} = 0.0027$ m/s, $u_{sl,b} = 0.00065$ m/s (max-min) and $u_{sl,b} = 0.00065$ m/s, $u_{sl,p} = 0.0013$ m/s (min-max) operations at $P = 0.1$, 0.8 and 2 MPa and $H = 0.65$ m.

[Color figure can be viewed in the online issue, which is available at wileyonlinelibrary.com.]

$\Gamma_{gl} a_{gl} \partial A_{gl}/\partial \epsilon_l$ or equivalently as $(P_g - P_l) + 1/\Pi_l \, \partial \epsilon_l/\partial t$. It can easily be recognized that the simulated gas, liquid and capillary pressure patterns verify the entropy inequality given by condition (C2) both under drainage ($P_g - P_l \geq P_c$ & $\partial \epsilon_l/\partial t \leq 0$) and imbibition ($P_g - P_l \leq P_c$ and $\partial \epsilon_l/\partial t \geq 0$) contexts. Also, a key feature stemming from Figure 11 suggests the system dynamics is characterized by a quite brief pressure relaxation time constant, i.e., $1/\Pi_l = o(\partial \epsilon_l/\partial t)$, hence, reestablishing sameness between $P_g - P_l$ and P_c nearly instantaneously. Therefore, assumption of static equilibrium is reasonable to account for interfacial forces and use of an *equilibrium* capillary pressure satisfying Eq. 25 is sufficient, i.e., $P_c = \rho_g \epsilon_g \partial A_g/\partial \epsilon_g - \rho_l \epsilon_l \partial A_l/\partial \epsilon_l - \Gamma_{gl} a_{gl} \partial A_{gl}/\partial \epsilon_l \approx P_g - P_l$.

Conclusion

The macroscopic nonequilibrium thermomechanical multiphase flow theory developed by Hassanizadeh and Gray for porous media was adapted and implemented for analyzing trickle-bed reactor hydrodynamics in unsteady-state conditions. In this nonequilibrium thermomechanical theory, the interfaces are treated as individual continua interacting and exchanging properties with the adjacent phase continua. As a prelude to modeling cyclic modulation in trickle beds, liquid holdup and pressure kinetics were measured and simulated in drainage and imbibition modes under different superficial (base-pulse) liquid and gas velocities.

The nonequilibrium two-phase flow model rests on inclusion of the following main features (1) conservation equations for gas-liquid interfacial area and interfacial momentum, (2) nonequilibrium capillary pressure, (3) Helmholtz free energy gradients in the body supply of momentum for fluid bulk phases and gas-liquid interface, and (4) mass exchange between interface and adjacent fluid bulk phases accounting for the production/destruction of gas-liquid interfacial area in the course of imbibition and drainage.

Constitutive relations were established for the macroscopic solid pressure, the macroscopic Helmholtz free energies, and the mass-exchange rates for production/destruction of interfacial area leading to more complete formulations of the dynamic capillary pressure and the body supplies of momentum. To solve the dynamic model, these constitutive relationships were calibrated using measurements of time varying liquid holdup (from electrical capacitance tomography) and bed-pressure drop. The developed constitutive equations verified the admissibility principle in accordance with the second law of thermodynamics.

Simulations from the standard two-phase flow model, relaxing the four aforementioned features (1 through 4), failed to capture the curvature of the liquid drainage curves although it restored very good estimations of the steady-state liquid holdups. The standard model predicted much slower drainage dynamics, especially as the contrast between pulse and base liquid velocities increased. On the other hand, simulations from the nonequilibrium two-phase flow model were compared to the liquid holdup and pressure drop transients during drainage and imbibition. Outperforming the standard model, the nonequilibrium model captured very well the pace of decay and breakthrough in drainage and imbibition. Its aptness to describe the transient hydrodynamics was attributed to inclusion of interfacial mass and momentum balance equations and of the new constitutive relations.

Close inspection of the nonequilibrium model outputs revealed that assumption of nonequilibrium capillary pressure in the studied range of experimental conditions was not necessary and static equilibrium described by $P_c \approx P_g - P_l$ was sufficient to account for the interfacial forces. However, recourse to empirical capillary relationships, such as the Leverett *J*-function, is unnecessary as this approach enables access to capillary pressure via entropy-consistent constitutive expressions for the macroscopic Helmholtz free energies. Also, the role of mass exchange between bulk fluid phase holdups and gas-liquid interfacial area was shown to play a non-negligible role in the dynamics of drainage and imbibition. By accounting for the production/destruction of interfacial area, they prompted much briefer response times for the system to attain steady state compared to the case without inclusion of these mass exchange rates.

Last but not least, the newly developed nonequilibrium model allows for a physically sound description of more complex dynamic phenomena such as trickle-bed periodic operation with liquid and gas-flow rate cyclic modulations. However, comparing macroscopic variables such as cross-sectionally averaged liquid holdup or bed overall pressure gradient is only a first step ahead with the confrontation of this new modeling approach. It has to be borne in mind that the model was tested in its 1-D version (stream-wise dependence only in dynamic mode). To capture microscale phenomena will require testing the model on larger scale trickle beds where indeed a radial property dependence of the hydrodynamic parameters may make sense so that a local probing technique that bears both space and time resolving capabilities will allow testing local features from the model and the experiments.

Acknowledgments

Financial support from the Natural Sciences and Engineering Research Council (NSERC) is gratefully acknowledged. FL expresses his appreciation to INP Toulouse & ENSIACET for the visiting professor fellowship.

Notation

a_s = external area of the bed, $a_s = 6(1-\varepsilon)/d_p$, m^2/m^3
$a_{\alpha\beta}$ = area of the $\alpha\beta$-interface per unit volume of porous medium, m^2/m^3
A = Helmholtz free energy function, m^2/s^2
d_p = particle diameter, m
$e^{\alpha}_{\alpha\beta}$ = rate of mass transfer from $\alpha\beta$-interface to the α-phase, kg/m^3 s
E_1, E_2 = Ergun constants
g = gravitational acceleration, m/s^2
P_α = pressure of α-fluid, Pa
P_c = capillary pressure, Pa
R_s = counteracting bed support (reaction) force, Pa/m
t = time, s
$T^{\alpha}_{\alpha\beta}$ = body supply of momentum to the α-phase from $\alpha\beta$-interface, Pa/m
$u_{s\alpha}$ = superficial velocity of α-fluid, m/s
v_α = interstitial velocity of α-fluid in z direction, m/s
w_{gl} = velocity of the gas-liquid interface, m/s
z = axial coordinate

Greek letters

β = parameter in Eq. 22
ϵ = bed porosity
ϵ_α = α-phase holdup
ε^*_l = liquid holdup which corresponds to maximum a_{gl} (ridge liquid holdup)
ϕ = parameter in Eq. 22
γ_{gl} = macroscopic interfacial tension of the gas-liquid interface, N/m
$\Gamma_{\alpha\beta}$ = macroscopic mass density of $\alpha\beta$-interface (excess mass of $\alpha\beta$-interface per unit area of $\alpha\beta$-interface), kg/m^2
λ = parameter characterizing the strength of change of specific gas-liquid interfacial area due to a change in liquid holdup
μ_α = α-phase dynamic viscosity, kg/ms
μ^e_α = α-phase effective viscosity (combination of bulk and shear terms), kg/ms
ρ_α = α-phase density, kg/m^3
$\tau^{\alpha}_{\alpha\beta}$ = nonequilibrium part of body supply of momentum to the α-phase from $\alpha\beta$-interface, kg/m^2s^2

Subscripts

g = gas phase
L = liquid phase
S = solid

Literature Cited

1. Dudukovic MP, Larachi F, Mills PL. Multiphase reactors - revisited. *Chem Eng Sci*. 1999;54:1975–1995.
2. Gupta R. Pulsed flow vapour-liquid reactor. US Patent 4, 526, 757,1985.
3. Haure PM, Hudgins RR, Silveston PL. Periodic operation of a trickle-bed reactor. *AIChE J*. 1989;35:1437–1444.
4. Lange R, Hanika J, Stradiotto D, Hudgins RR, Silveston PL. Investigation of periodically operated trickle-bed reactors. *Chem Eng Sci*. 1994;49:5615–5621.
5. Lange R, Schubert M, Dietrich W, Grünewald M. Unsteady-state operation of trickle-bed reactors. *Chem Eng Sci*. 2004;59:5355–5361.
6. Khadilkar M, Al-Dahhan MH, Dudukovic MP. Parametric study of unsteady-state flow modulation in trickle-bed reactors. *Chem Eng Sci*. 1999;54:2585–2595.
7. Wilhite BA, Huang X, McCready MJ, Varma A. Effects of induced pulsing flow in trickle-bed reactor performance. *Ind Eng Chem Res*. 2003;42:2139–2145.
8. Boelhouwer JG, Piepers HW, Drinkenburg AAH. Advantages of forced non-steady operated trickle-bed reactors. *Chem Eng Technol*. 2002;25:647–650.
9. Hamidipour M, Larachi F, Ring Z. Monitoring filtration in trickle beds using electrical capacitance tomography. *Ind Eng Chem Res*. 2009;48:1140–1153.
10. Aydin B, Hamidipour M, Larachi F. Fast mode alternating cyclic operation in trickle beds at elevated temperature for foaming systems. *Chem Eng Sci*. 2007;62:7539–7547.
11. Boelhouwer JG, Piepers HW, Drinkenburg AAH. Liquid-induced pulsing flow in trickle-bed reactors. *Chem Eng Sci*. 2002;57:3387–3399.
12. Giakoumakis D, Kostoglou M, Karabelas AJ. Induced pulsing in trickle beds - characteristics and attenuation of pulses. *Chem Eng Sci*. 2005;60:5183–5197.
13. Aydin B, Fries D, Lange R, Larachi F. Slow-mode induced pulsing in trickle-bed reactors at elevated temperature. *AIChE J*. 2006;52:3891–3901.
14. Aydin B, Fries D, Lange R, Larachi, F. Slow-mode induced pulsing in trickle beds at elevated temperature for (non-)Newtonian liquids. *Chem Eng Sci*. 2007;62:5554–5557.
15. Aydin B, Larachi F. Structure of trickle-to-pulse flow regime transition and pulse dynamics at elevated temperature in slow-mode cyclic operation. *Chem Eng Sci*. 2008;63:1510–1522.
16. Janecki D, Burghardt A, Bertelmus G. Computational simulations of the hydrodynamic parameters of a trickle-bed reactor operating at periodically changing feeding the bed with liquid. *Chem Process Eng*. 2008;29:583–596.
17. Atta A, Hamidipour M, Roy S, Nigam KDP, Larachi F. Propagation of slow/fast-mode solitary liquid waves in trickle beds via electrical capacitance tomography and computational fluid dynamics. *Chem Eng Sci*. 2010;65:1144–1150.
18. Hassanizadeh SM, Gray WG. Mechanics and thermodynamics of multiphase flow in porous media including interphase boundaries. *Adv Water Resour*. 1990;13:169–185.
19. Gray WG, Hassanizadeh SM. Macroscale continuum mechanics for multiphase porous-media flow including phases, interfaces, common lines and common points. *Adv Water Resour*. 1998;21:261–281.
20. Gray WG, Hassanizadeh SM. Unsaturated flow theory including interfacial phenomena. *Water Resour Res*. 1991;27:1855–1863.
21. Achanta A, Cushman JH, Okos MR. On multicomponent, multiphase thermomechanics with interfaces. *Int J Eng Sci*. 1994;32:1717–1738.
22. Attou A, Ferschneider G. A two-fluid model for flow regime transition in gas-liquid trickle-bed reactors. *Chem Eng Sci*. 1999;54:5031–5037.
23. Hassanizadeh SM, Gray WG. Toward an improved description of the physics of two-phase flow. *Adv Water Resour*. 1993;16:53–67.
24. Hassanizadeh SM, Gray WG. Thermodynamic basis of capillary pressure in porous media. *Water Resour Res*. 1993;29:3389–3405.
25. Levec J, Grosser K, Carbonell R. The hysteretic behavior of pressure drop and liquid holdup in trickle beds. *AIChE J*. 1988;34:1027–1030.
26. Maiti R, Khanna R, Nigam KDP Hysteresis in trickle bed reactors: A review. *Ind Eng Chem Res*. 2006;45:5185–5198.
27. Niessner J, Hassanizadeh SM. A model for two-phase flow in porous media including fluid–fluid interfacial area. *Water Resour Res*. 2008;44:W08439.
28. Niessner J, Hassanizadeh SM. Non-equilibrium interphase heat and mass transfer during two-phase flow in porous media - Theoretical considerations and modeling. *Adv Water Res*. 2009;32:1756–1766.
29. Culligan KA, Wildenschild D, Christensen BS, Gray WG, Rivers ML, Tompson AFB. Interfacial area measurements for unsaturated flow through porous media. *Water Resour Res*. 2004;40:W12413.
30. Dankworth DC, Kevrekidis IG, Sundaresan S. Dynamics of pulsing in trickle beds. *AIChE J*. 1990;36:605–621.
31. Iliuta I, Ortiz, A, Larachi F, Grandjean BPA, Wild G. Hydrodynamics & mass transfer in trickle-bed reactors: an overview. *Chem Eng Sci*. 1999;54:5329–5337.
32. Iliuta I, Grandjean BPA, Larachi F. New mechanistic film model for pressure drop and liquid holdup in trickle flow reactors. *Chem Eng Sci*. 2002;57:3359–3371.
33. Hamidipour M, Larachi F. Modulation of suspension electrical conductivity to counter fines plugging in trickle-bed reactors. *AIChE J*. 2011;57:1829–1839.
34. Schubert M, Hamidipour M, Duchesne C, Larachi F. Hydrodynamics of co-current two-phase flows in slanted porous media - Modulation of pulse flow via bed obliquity. *AIChE J*. 2010;56:3189–3205.
35. Grosser KA, Carbonell RG, Sundaresan S. The transition to pulsing flow in trickle beds. *AIChE J*. 1988;34:1850–1860.

Manuscript received July 7, 2011 and revision received Oct. 17, 2011.